Persistent and Partially Mobile Oxygen Vacancies in Li-Rich Layered Oxides

Peter M. Csernica[1], Samanbir S. Kalirai[1,2], William E. Gent[1], Kipil Lim[1,3], Young-Sang Yu[2], Yunzhi Liu[1], Sung-Jin Ahn[4], Emma Kaeli[1], Xin Xu[1], Kevin H. Stone[3], Ann F. Marshall[5], Robert Sinclair[1], David A. Shapiro[2*], Michael F. Toney[3,6*], and William C. Chueh[1,7*]

[1]*Department of Materials Science and Engineering, Stanford University, Stanford, CA 94305, USA.*

[2]*Advanced Light Source, Lawrence Berkeley National Laboratory, Berkeley, CA 94720, USA.*

[3]*Stanford Synchrotron Radiation Lightsource, SLAC National Accelerator Laboratory, 2575 Sand Hill Road, Menlo Park, CA 94025, USA.*

[4]*Energy Lab., Samsung Advanced Institute of Technology, 130, Samsung-ro, Yeongtong-gu, Suwon-si, Gyeonggi-do 16678, South Korea.*

[5]*Stanford Nano Shared Facilities, Stanford University, Stanford, CA 94305, USA.*

[6]*Department of Chemical and Biological Engineering, University of Colorado Boulder, Boulder CO 80309, USA*

[7]*Stanford Institute for Materials and Energy Sciences, SLAC National Accelerator Laboratory, Menlo Park, CA 94025, USA.*

* Corresponding authors: dashapiro@lbl.gov, mftoney@slac.stanford.edu, wchueh@stanford.edu

Abstract

Increasing the energy density of layered oxide battery electrodes is challenging as accessing high states of delithiation often triggers voltage degradation and oxygen release. Here, we utilize transmission-based X-ray absorption spectromicroscopy and ptychography on mechanically cross-sectioned $Li_{1.18-x}Ni_{0.21}Mn_{0.53}Co_{0.08}O_{2-\delta}$ electrodes to quantitatively profile the oxygen deficiency over cycling at the nanoscale. The oxygen deficiency penetrates into the bulk of individual primary particles (~ 200 nm) and is well-described by oxygen vacancy diffusion. Using an array of characterization techniques, we demonstrate that, surprisingly, bulk oxygen

vacancies which persist within the native layered phase are indeed responsible for the observed spectroscopic changes. We additionally show that the arrangement of primary particles within secondary particles (~ 5 μm) causes significant heterogeneity in the extent of oxygen release between primary particles. Our work merges an ensemble of length-spanning characterization methods and informs promising approaches to mitigating the deleterious effects of oxygen release in lithium-ion battery electrodes.

Introduction

Two of the primary challenges facing the commercialization of lithium- and manganese-rich (LMR) materials are the progressive fading of the discharge voltage over cycling[1–7] and their tendency to release oxygen at high states of delithiation. While oxygen release in layered oxides has been extensively studied on the first electrochemical cycle, less is known about the process over extended cycling. This is partly due to the fact that, in contrast to the first cycle, only small quantities of oxygen are released in each subsequent cycle such that negligible signal can be detected in electrochemical mass spectrometry studies[8–10]. Additionally, it remains challenging to reconcile nanoscale observations, some of which suggest significant mass loss and Li depletion coincident with a release of nearly one-fifth of the oxygen[11], with cell-level observations of negligible capacity fade over 100+ cycles[11,12,13]. Nevertheless, oxygen release during extended cycling has recently been proposed to be the underlying cause of the voltage fade, as it activates lower-voltage redox couples[12,14] and is believed to inevitably cause pernicious phase transitions[7,15]. Therefore, in order to develop practical strategies for mitigating both oxygen release and voltage decay in LMR materials, several aspects of the oxygen release phenomenon must be clarified.

First, the ability of these materials to transport oxygen at room temperature is uncertain, and thus it is unclear whether the oxygen deficiency is limited to the near-surface (a few nm) region[9,16,17] or penetrates into the bulk of primary particles (hundreds of nm) after many cycles[11]. Second, due to a gap in length scales accessed by standard analytical techniques, the influence of microstructure on the heterogeneity of oxygen release has not been assessed. Third, there is significant confusion over the structural implications of oxygen release during extended cycling. The established view, supported primarily from local TEM observations[7,15], is that oxygen release is invariably associated with a phase transition to a more transition-metal-rich phase (e.g. a spinel or 'spinel-like' phase)[7,15,16,18–21]. However, bulk-sensitive XRD studies often do not show the growth of new peaks indicative of a macroscopic phase transformation[2,5], calling into question whether bulk phase transformations indeed govern the behavior of LMR layered oxides. Finally, it remains ambiguous whether oxygen release is simply correlated with the commonly observed bulk cation disordering (within the native layered phase)[3,5] or if there exists a mechanistic relationship between the two phenomena.

In this work, we obtain oxidation state maps spanning interfaces (~ 10 nm), primary particles (~ 200 nm), secondary particles (~ 5 μm), and the entire electrode thickness (> 40 μm) using nanoscale X-ray spectromicroscopy and ptychography on electrodes sectioned by solvent-free ultramicrotomy. These quantitative maps reveal that oxygen originating in the bulk of primary particles is eventually released over hundreds of cycles at room temperature. The oxygen deficiency profiles suggest that oxygen vacancy diffusion, as opposed to a phase transition, likely governs oxygen release in $Li_{1.18-x}Ni_{0.21}Mn_{0.53}Co_{0.08}O_{2-\delta}$ (LMR-NMC). The existence of bulk oxygen vacancies which persist within the native layered phase is confirmed by additional chemical and structural analysis, overturning the prevailing view that oxygen release

is necessarily accompanied by a phase transition. This result also contradicts the suspicion that oxygen vacancies, if present, will inevitably undergo vacancy condensation and be eliminated from the lattice[11]. Importantly, the existence of bulk oxygen vacancies provides a plausible atomistic explanation linking progressive oxygen release to progressive single-phase cation disordering[3,5], unifying two previously proposed explanations for the voltage decay. Finally, we reveal that the extent of oxygen release for an individual primary particle depends strongly on the surrounding secondary structure, with those residing in the interior of large secondary particles being more protected from oxygen release. These results together inform new chemical, structural, and morphological strategies for preventing oxygen release in layered oxide positive electrodes.

Cation Disordering and Reduction Over Cycling

Uncoated LMR-NMC electrodes were cycled in full cells against graphite (Samsung mini-18650, see Methods). Electrodes were harvested at various cycle numbers and assembled into half cells where they were cycled once more against Li metal. Figure 1a shows charging and discharging at ~ 4 mA g^{-1} in a half cell after up to 500 full cell cycles (see Methods). With cycling, the quasi-open-circuit voltage of various redox processes decreases on both charge and discharge, implying that significant changes occur in the bulk of the material[5]. Despite these changes, however, the capacity fade is minimal, with the electrode retaining 96% of its initial low-rate discharge capacity (Supplementary Fig. 1). The stable low-rate discharge capacity suggests that the Li content of electrodes discharged at low rate (in a half cell) is similar regardless of cycle number, which we confirm directly through inductively coupled plasma mass spectroscopy (ICP-MS, Supplementary Fig. 2).

Rietveld refinement of synchrotron powder X-ray diffraction (SXRD) patterns reveals that LMR-NMC remains single phase with the $R\bar{3}m$ space group after 500 cycles with no tetrahedral occupancy of transition metals (Fig. 1b, Supplementary Fig. 3–6). The lack of secondary crystallographic phases is also supported by selected area electron diffraction (Supplementary Figure 7) and high-resolution transmission electron microscopy (Supplementary Figures 8 and 9). Interestingly, Rietveld refinement does show that the transition metal (TM) occupancy in Li layer octahedral sites increases steadily from 2 to 10 at. % with cycling (Fig. 1c), consistent with previous reports[5,22].

We additionally probed the spatially-averaged electronic structure[23] using transmission-based TM K-edge X-ray absorption spectroscopy (XAS) (Supplementary Figs. 10–12). With cycling, Mn and Co are progressively reduced from their initial Mn^{4+} and Co^{3+} states while Ni remains in its initial Ni^{2+} state (Fig. 1c). Given that the Li content in each sample is approximately identical and that the crystallographic phase of the material is unchanged, we infer from bulk electroneutrality that the spectroscopic changes here correspond to oxygen release[12]. This conclusion is also consistent with the SXRD Rietveld refinements[24] (Supplementary Figs. 3 and 13) and nanoscale oxidation state maps, which are discussed below. Interestingly, the reduction of Mn and Co over cycling can be partially reversed by conducting a low-temperature heat treatment at 150 °C in 100% O_2 (Fig. 1c). We will discuss this intriguing result in detail later.

The TM oxidation states from XAS were used to estimate the fraction of oxygen release relative to the pristine material: ~ 3.3 at. % after the first cycle (which is preceded by formation cycling) and ~ 6.5 at. % after 500 cycles (Supplementary Note 1). The large first-cycle oxygen release is consistent with the findings of previous gas analysis experiments[16,25,26]. Our XAS

126 results, taken together with our findings from SXRD, reveal that both phenomena previously
127 linked to voltage fade—progressive cation disordering and progressive oxygen release—occur
128 simultaneously over extended cycling. The strong correlation observed here (Fig. 1c) suggests
129 that the two may be mechanistically linked to one another, a point which we will return to later.

130 To map oxygen loss at the nanoscale, we utilized soft X-ray scanning transmission X-ray
131 microscopy (STXM) and X-ray ptychography at the Advanced Light Source, the latter with
132 greater spatial resolving power[27–30]. Using these two transmission-based microscopy techniques
133 in spectro-microscopy mode, we probed the TM L_3 absorption edges and the oxygen K edge
134 without self-absorption effects. With cycling, Mn and Co reduction are both observed in the
135 averaged (Supplementary Methods) L_3 edge spectra, whereas no change was observed at the Ni
136 L_3 edge[2] (Supplementary Fig. 14–17). These spectral changes, visible from the difference plots
137 even without quantification (Fig. 1d), are in strong agreement with TM K-edge spectroscopy
138 results, providing unambiguous evidence that the *d* electron count increases with cycling.

139 **Oxidation State Heterogeneity within Primary Particles**

140 As in most layered oxides, primary particles in LMR-NMC exist in secondary particle
141 agglomerates (~ 5 μm) rather than as isolated particles. To preserve the secondary structure
142 while also making the sample sufficiently transparent to soft X-rays, thin cross-sectional
143 lamellae were prepared by dry mechanical ultramicrotomy (Supplementary Fig. 18, Methods).
144 We first discuss the oxidation state heterogeneity within individual primary particles using X-ray
145 spectro-ptychography at the Mn L_3 edge, which has a resolution of ~ 5–20 nm (Fig. 2a–c,
146 Supplementary Fig. 19). As expected, the Mn reduction after a single cycle is concentrated near
147 the particle edges, indicating that oxygen release initiates at the surface of particles (Fig. 2d,

148 Supplementary Figs. 20 and 21). This observation spatially decouples first-cycle oxygen release,
149 which is concentrated at surfaces, from oxidized lattice oxygen[31], which charge compensates the
150 majority of the capacity in the first-cycle voltage plateau and exists throughout the particle bulk
151 even on the initial cycle[2]. Additionally, there is significant heterogeneity in the extent of oxygen
152 release between primary particles (Fig. 2b), which we will return to later. Finally, oxygen
153 deficiency that begins on the particle surface progressively enters (> 100 nm) into the bulk
154 material over many electrochemical cycles (Fig. 2d). This observation is consistent with previous
155 electron[13] and X-ray[32] microscopy studies showing TM reduction beyond the surface of LMR
156 particles.

157 The quantitative nature of the oxidation state maps of primary particles allows us to
158 directly evaluate two mechanistic possibilities. The first is single-phase oxygen ambipolar
159 diffusion from the bulk to the particle surface. The second is a two-phase (core-shell)
160 reaction[21,33,34], in which a new phase with a more reduced Mn oxidation state grows inwards
161 from the surface. Figure 2e,g shows three independent fittings to the Mn^{3+} concentration profiles
162 of individual particles for each of the two models (Supplementary Note 2). The fits utilizing a
163 two-phase reaction are poor, as a depth-averaged core-shell model predicts a constant Mn^{3+}
164 concentration in the shell which is not observed experimentally. Conversely, the individual
165 particle fits utilizing the vacancy diffusion model describe the data reasonably well
166 (Supplementary Figure 22), suggesting that oxygen chemical diffusion governs bulk oxygen
167 release in LMR-NMC.

168 Quantitatively, the fitting (Supplementary Note 2) gives room-temperature oxygen
169 chemical diffusivities (D_O) within an order of magnitude of 10^{-17} cm^2 s^{-1} in the delithiated state,
170 where oxygen is known to be most mobile[35,36]. This room-temperature oxygen chemical

diffusion coefficient, although large enough to cause bulk oxygen depletion over extended cycling, is six to seven orders of magnitude lower than those of some fast oxygen-ion-conducting perovskite oxides[39–42]. Several factors may contribute to oxygen transport in LMR-NMC. Since LMR-NMC is known to have oxidized oxygen species at high extents of delithiation (such as molecular O_2, O_2^{2-}, or O^-)[2,43], the diffusing species may in fact be a less ionized oxygen which could be more mobile[44,45] than O^{2-}. Extended defects such as dislocations may also contribute[46,47]. We note that although fitting with a constant oxygen chemical diffusivity gives good fits to the data, the true chemical diffusivity is likely not constant during cycling due to progressive changes in the material structure. For completeness, we also performed STXM imaging on dispersed[2] (rather than cross-sectioned) samples, which are consistent with the conclusion of bulk oxygen release (Supplementary Figs. 16 and 17).

The Existence of Bulk Oxygen Vacancies

Although the spatial analysis of Mn^{3+} concentration suggests oxygen vacancies may be present in the bulk material, proof of this remains lacking because neither XAS nor SXRD can directly resolve the anion sublattice. Given that LMR-NMC remains single phase over cycling, we consider two structural models[24,48] for the electrode after 500 cycles (Fig. 3a). The first involves an anion sublattice with vacancies that persist over many cycles, which we refer to as the oxygen vacancy structure ($[Li_{1.18}TM_{0.82}]\,[O_{1.87}\square_{0.13}]$, where the first and second brackets define the cation and anion sublattice, respectively). Here, the point defect reaction governing the changes over cycling in the lithiated material can be written in Kröger-Vink notation as:

$$4TM_{TM}^{\times} + 2O_O^{\times} \rightarrow 2V_O^{\cdot\cdot} + 4TM_{TM}' + O_2(g) \qquad [1]$$

The second structural model involves a fully occupied anion sublattice referred to as the densified structure ($[Li_{1.06}TM_{0.94}][O_2]$), whereby the evolved oxygen causes TMs at the surface to back diffuse into the bulk[19,21,49–51]. The analogous point defect reaction can be written as:

$$3TM_{TM}^{\times} + 2Li_{Li}^{\times} + 2O_O^{\times} \rightarrow 2TM_{TM}' + TM_{Li}^{\cdot\cdot\cdot} + 2Li + O_2(g) \qquad [2]$$

These two structure models are indistinguishable using XAS, as both models can explain a reduction in the average TM oxidation state (Fig. 3a). They are also nearly indistinguishable with neutron diffraction (Supplementary Fig. 23) or SXRD[24,48] (Supplementary Fig. 24).

Crucially, the predominant difference between the two structure models is that the densified structure has a considerably lower Li to TM elemental ratio (Li:TM) of 1.12 while the oxygen vacancy structure has a Li:TM of 1.44 (Supplementary Note 3). Figure 3b shows that, consistent with the meager capacity fade observed both here and elsewhere[11,12,13], the Li:TM of electrodes discharged to and held at 2.5 V vs. Li/Li^+ is nearly constant with cycling, indicating that bulk densification is only a minor contributor (~ 15% if the entire decrease in Li:TM and electrochemical capacity is due to densification) to the structure of the cycled material. We note that while the cathode electrolyte interphase (CEI) may contribute to the ICP-MS signal, the CEI would have to contain 22.5% of the Li content of LMR-NMC (after 500 cycles, discharged in a half cell) and no TMs to explain the ICP-MS results with the densified structure. As a recent cryo-EM study has shown that CEI on Li-rich materials is essentially non-existent[52], we therefore conclude that contrary to earlier reports[7,48,49], the bulk oxygen vacancy structure is far more likely to explain both the nearly constant Li:TM over extended cycling as well as the stable electrochemical capacity (Supplementary Note 4).

The material density also contrasts significantly between the two structural models, with the predicted densities differing by nearly 10% after 500 cycles (Supplementary Note 5). Therefore, we utilized helium gas pycnometry, which has been used previously to measure cation vacancy concentrations in layered oxides[53], to determine the density of LMR-NMC with cycling. The experimental results agree reasonably well with the density changes predicted by the oxygen vacancy structure model, providing more support for the existence of oxygen vacancies (Fig. 3b). We note that the presence of closed pores may complicate the interpretation of the pycnometry measurement, a point which is discussed thoroughly in Supplementary Note 6 (also see Supplementary Figures 25–27).

As a final piece of evidence, we return to the oxidation of TMs upon annealing the cycled material (Fig. 1c, Supplementary Figure 28), a similar experiment to those conducted in several recent works[47,54] (see Supplementary Note 7). In addition to TM K edge XAS, evidence for TM oxidation includes TM K edge extended X-ray absorption fine structure (EXAFS) data, Rietveld refinement, and electrochemical analysis (Supplementary Figures 3, 29– 31). The TM oxidation during annealing could come from a change in either the Li or O stoichiometry. If the densified structure were operative *before* the annealing process, an increase in the oxygen stoichiometry would have to proceed via the insertion of oxygen interstitials:

$$4\mathrm{TM}_{\mathrm{TM}}^{'} + \mathrm{O}_2(\mathrm{g}) \rightarrow 4\mathrm{TM}_{\mathrm{TM}}^{\times} + 2\mathrm{O}_{\mathrm{i}}^{''} \qquad [3]$$

In addition to being intuitively unlikely, the insertion of oxygen interstitials almost certainly would expand the lattice rather than resulting in the contraction that is experimentally observed. Alternatively, Li could be removed from the structure during annealing via the following reaction, where Li on the product side is some Li containing compound (e.g. Li_2O):

$$2\mathrm{Li}_{\mathrm{Li}}^{\times} + 2\mathrm{TM}_{\mathrm{TM}}' \rightarrow 2\mathrm{TM}_{\mathrm{TM}}^{\times} + 2\mathrm{V}_{\mathrm{Li}}' + 2\mathrm{Li} \quad [4]$$

This process, representing lithium loss of a slightly less Li-rich (than the pristine material) oxide in the absence of electrolyte at 150° C, is also extremely unlikely. We can therefore conclude that the densified structure is a poor explanation for the structure of the material *prior* to annealing.

Conversely, if the oxygen vacancy structure were operative, an increase in the oxygen stoichiometry could proceed via the refilling of previously formed oxygen vacancies:

$$2\mathrm{V}_{\mathrm{O}}^{\cdot\cdot} + 4\mathrm{TM}_{\mathrm{TM}}^{'} + \mathrm{O}_2(\mathrm{g}) \rightarrow 4\mathrm{TM}_{\mathrm{TM}}^{\times} + 2\mathrm{O}_{\mathrm{O}}^{\times} \quad [5]$$

Additionally, a decrease in Li stoichiometry may be possible, as oxygen vacancies present *before* the annealing process could combine with Li vacancies formed via eqn. (4):

$$\mathrm{TM}_{\mathrm{TM}}^{\times} + 2\mathrm{V}_{\mathrm{Li}}' + 2\mathrm{V}_{\mathrm{O}}^{\cdot\cdot} \rightarrow \mathrm{TM}_{\mathrm{Li}}^{\cdot\cdot} \quad [6]$$

Eqn. 6, while potentially being kinetically inhibited at room temperature, should be thermodynamically favorable, as the elimination of oxygen vacancies would restore undercoordinated transition metals to their full coordination[20]. Combining eqn. (4) and eqn. (6) results in a net defect reaction which could cause TM oxidation if oxygen vacancies are present *before* annealing, where Li on the product side is some Li containing compound (e.g. Li_2O):

$$2\mathrm{Li}_{\mathrm{Li}}^{\times} + 2\mathrm{TM}_{\mathrm{TM}}' + 2\mathrm{V}_{\mathrm{O}}^{\cdot\cdot} \rightarrow \mathrm{TM}_{\mathrm{TM}}^{\times} + \mathrm{TM}_{\mathrm{Li}}^{\cdot\cdot} + 2\mathrm{Li} \quad [7]$$

Because of the thermodynamic favorability of eqn. (6), eqn. (7) is much more plausible alternative to eqn. (4). Thus, regardless of whether a change in the Li or O stoichiometry governs the TM oxidation, the oxygen vacancy structure is far more likely to explain the material *before* annealing.

We emphasize that in the above discussion (summarized in Supplementary Table 1) we were concerned with the structural changes occurring in the bulk of the material rather than in the near-surface region (a few nm), as many works have reported a densified surface layer that does not significantly change in thickness during cycling[7,19,37,38].

Oxygen Vacancies and the Cation Sublattice

The existence of bulk oxygen vacancies confirms that single-phase vacancy diffusion is responsible for the Mn^{3+} concentration profiles within primary particles (Fig. 2). This overturns the accepted view that bulk oxygen release kinetics in LMR-NMC are necessarily governed by phase transitions[12]. Furthermore, bulk oxygen vacancies provide an atomistic link between single-phase cation disordering and oxygen release, both of which occur progressively with cycling and have been independently proposed as the reason for the voltage decay[5,12]. Namely, an oxygen vacancy will cause neighboring TMs to become undercoordinated and therefore more likely to move to alternative lattice sites. We note that this explanation was previously suggested to be responsible for the observed surface densification process[13,17,19,58]. Cation disordering may also promote oxygen vacancy formation, allowing the lattice to more easily accommodate and/or transport an oxygen vacancy. This coupling suggests that the strategic prevention of either of these phenomena may enhance electrochemical performance in part due to the coupling between them. Indeed, surface modifications designed to prevent oxygen release mitigate both voltage decay and cation disordering[14,15,59,60]. Likewise, modified stacking sequences or large interlayer spacings which restrict TM mobility mitigate both voltage decay[55,61,62] and oxygen release[62,63].

As a final point of interest, EXAFS data (Fig. 3c) show a decrease in the scattering intensity of the first coordination shell with cycling for both Mn and Co, but not Ni. This

decrease in intensity can originate from the formation of both $V_O^{\cdot\cdot}$ and $TM_{Li}^{\cdot\cdot}$ (Fig. 3d, Supplementary Fig. 32), although a disorder in the first shell M–O bond distances due to the loss of in-plane ordering or the fractional average oxidation states of Mn and Co may also contribute. However, the Ni first shell scattering intensity remains higher than would be predicted based on a random distribution of both $V_O^{\cdot\cdot}$ and $TM_{Li}^{\cdot\cdot}$. Therefore, we hypothesize that the oxygen vacancies may preferentially form around Mn and Co, the same atoms which undergo TM reduction (Supplementary Note 8). The EXAFS data additionally suggest that if Ni atoms migrate during delithiation, as has been suggested from previous EXAFS data[2], these migrations may be more reversible than those of Mn and Co. We speculate that this may be due to the large change in ionic radius Ni experiences during cycling, as the sites Ni^{4+} migrates into on delithiation may not be suitable for the Ni^{2+} which forms on lithiation.

Importance of Secondary Particle Microstructure

Although cross-sectioning the electrode into nominally 80 nm-thick lamellae cuts through secondary particles, some information about the location of a given primary particle within the secondary structure can be inferred. Specifically, large agglomerates in the lamella represent cross-sections that went through the center of large secondary particles. Smaller agglomerates could either represent a cross-section closer to the secondary particle edge or through the center of a smaller secondary particle (Supplementary Fig. 18).

Mn oxidation state maps after one cycle were obtained via STXM at the electrode level (~ 50 × 50 μm, Fig. 4a) as well as that of a single large agglomerate with finer resolution (~ 5 × 5 μm, Fig. 4b). Figure 4b reveals that the primary particles inside of the large agglomerate are significantly more oxidized, and thus release less oxygen, than those outside of the agglomerate.

Figure 4c quantitatively demonstrates that this trend is preserved even when controlling for the pixel-wise thickness of the primary particle being examined (Supplementary Fig. 33). This implies that even primary particles of identical size will exhibit a degree of oxygen release that is heavily dependent on their location within the secondary structure. Additionally, Fig. 4b shows that within the large agglomerate, primary particles near the exterior are more reduced than those on the interior (Fig. 4b,d , Supplementary Fig. 34). Taken together, these findings reveal that primary particles originating from the interior of large secondary particles release comparably less oxygen. Conversely, primary particles originating from either the exterior of large secondary particles or from small secondary particles release a relatively large quantity of oxygen. Both of these observations are quantitatively supported by investigation of an ensemble of large agglomerates (Fig. 4a,d , Supplementary Figs. 35–37).

Interestingly, the fact that the Mn^{3+} distribution in each individual primary particle (Fig. 2a–c) is nearly radial indicates that each primary particle releases oxygen from its surface. Therefore, the observed heterogeneity cannot be explained by differences in the effective oxygen diffusion length among primary particles, as would occur if oxygen release occurred entirely from the secondary particle surface (Supplementary Fig. 38). Although the fundamental reason for the heterogeneity is still under investigation, one possibility is that stress buildup in large secondary particles[64] could modify the local oxygen chemical potential and/or diffusivity. Diminished electrolyte-induced oxygen release for interior primary particles is also possible, although electrolyte penetration into the secondary particle interior may also occur[65,66].

Regardless of the underlying cause, the observed heterogeneity shows that many primary particles must be examined to arrive at robust conclusions (Supplementary Fig. 39). The results additionally suggest that larger secondary particles, with the primary particle size held constant,

are expected to exhibit less oxygen release and possibly greater voltage retention. While this improvement may come at the expense of usable capacity and/or rate capability, spectromicroscopy analysis of delithiated samples suggests that large secondary particles may achieve Li contents comparable to those of smaller secondary particles (Supplementary Fig. 40). Previous work also suggests that the primary particle size may be a more important factor in determining the achievable capacity[65,67]. The possibility of cycling a similar quantity of Li while simultaneously mitigating oxygen release advocates for the exploration of larger LMR-NMC secondary particles.

Spectroscopic Analysis of the Delithiated State

While the Mn L_3-edge XAS shows progressive reduction with cycling in the discharged state, all LMR-NMC electrodes charged to 4.6 V exhibited a uniform Mn^{4+} oxidation state, even after 500 cycles (Supplementary Fig. 41). This finding verifies the emergence of a reversible $Mn^{3/4+}$ redox couple upon cycling[12,16] and further confirms that the bulk Mn reduction observed in the discharged state cannot be due to an electrochemically-inactive second phase.

Conversely, oxidation state maps at the Ni L_3 edge show the opposite behavior. While the Ni oxidation state remains uniform in the discharged electrodes with cycling (Supplementary Fig. 42 and 43), it is heterogeneous in the charged electrodes (Fig. 5). Specifically, Figure 5d shows that thicker regions reach a higher oxidation state than thinner regions[2]. This heterogeneity is not likely due to sluggish Li^+ transport both because of the long constant voltage hold and the fact that thicker regions would be expected to be less oxidized if transport were limiting. Instead, the lower oxidation state of thinner regions may be due to the fact that thinner are expected to have more reduced Mn in the discharged state (Fig. 2d, 4c). This allows Mn to

compensate more charge during delithiation, requiring less charge compensation from Ni. Additionally it is known that the atomic structure at the surface of the particle (~ 5 nm) reconstructs significantly due to interactions with the electrolyte[38]. This modified surface structure may not cycle as much Li and is generally more reduced than the bulk material[38], which may also contribute to the observed thickness dependence.

Interestingly, the O K-edge spectra, like the Ni L_3-edge spectra, are uniform in the discharged state (Supplementary. Figs. 42 and 44) but exhibit heterogeneity at 4.6 V (Fig. 5c). As shown in Fig. 5d, the O and Ni oxidation state exhibit a similar dependence on particle thickness, likely for the same reasons described earlier. The significant amounts of Ni and O oxidation observed[68], particularly for thicker regions where the LMR-NMC bulk is responsible for the majority of the signal, indicate that the existence of bulk oxygen vacancies does not inhibit the redox of either of these elements. This observation is consistent with the negligible capacity fade after 500 cycles.

Implications for Oxygen Release Mitigation

Substantial effort has been devoted to the mitigation of oxygen release in layered oxide positive electrodes. By a large margin, the most common approach to resolving this issue is to apply surface treatments to the electrodes[14,15,59,60,69,70]. However, additional approaches should also be considered, particularly because they could work synergistically with an appropriate surface coating. Our results, obtained from an industrially-relevant LMR-NMC material, suggest several additional strategies which have not been adequately examined. First, chemical or structural modifications which can decrease the oxygen chemical diffusivity, a property which is crucial but hardly understood[51] in Li-ion layered oxides, should be explored. Second, the

prevention of cation disordering, which is inhibited in many Na-ion materials due to their large interlayer spacing and unique stacking order[71], is another important strategy which may inhibit the structural changes necessary to accommodate an oxygen vacancy. This route has been shown to successfully mitigate oxygen release in Na-ion materials even when they undergo a phase transition involving layer sliding[62,63]. Finally, our results suggest that morphological control is a potential chemistry-agnostic method to achieve stability against oxygen release. For LMR oxides specifically, larger secondary particles, with the primary particle size held constant, may mitigate the oxygen release problem while preserving electrochemical capacity[65].

Conclusions

Using X-ray spectromicroscopy and ptychography, we showed that bulk lattice oxygen is released in significant quantities during extended cycling. The extent of oxygen release for an individual primary particle was found to be highly dependent on its location within the secondary structure, offering opportunities for morphological mitigation of the oxygen release phenomenon. While oxygen release is typically associated with a phase transition between two or more phases each containing a full anion sublattice, we demonstrate here that only a small amount (~ 15%) of material densification occurs, likely at the very surfaces of primary particles. Instead, surprisingly, the majority of oxygen release over cycling creates bulk oxygen vacancies which form and persist within the native layered phase. These vacancies, created at the primary particle surface, enter into the bulk over extended cycling with a fitted oxygen chemical diffusivity of $\sim 10^{-17}$ cm^2 s^{-1} in the delithiated state. Our observations unify previous observations of TM reduction and single-phase cation disordering and imply that cycling-induced oxygen release can be mitigated via chemical or structural modifications which inhibit the formation and/or transport of oxygen vacancies within the bulk material.

Methods

Materials. The $Li_{1.18}Mn_{0.53}Ni_{0.21}Co_{0.08}O_2$ materials were synthesized as previously reported[2]. In short, $Mn_{0.53}Ni_{0.21}Co_{0.08}(OH)_2$ precursor powder was synthesized by coprecipitation of stoichiometric quantities of $NiSO_4$, $CoSO_4$, and $MnSO_4$. The precursor was then mixed with the appropriate amount of Li_2CO_3 and calcined at 900 °C for 10 h to obtain powder of the target composition, $Li_{1.18}Mn_{0.53}Ni_{0.21}Co_{0.08}O_2$. We used this target composition for all calculations in the text.

Electrochemical measurements. All samples that are not labeled as "Pre-Formation" were first subject to electrochemical cycling inside mini-18650 cells (Samsung) containing a 92% LMR-NMC, 4% carbon, and 4% binder composite by mass as the positive electrode and graphite as the negative electrode. The cells used a 1.3 M $LiPF_6$ in 3:8:9 (vol/vol/vol) fluoroethylene carbonate (FEC)/ hydrofluoro ether (HFE)/dimethyl carbonate (DMC) electrolyte with some proprietary additives. This cycling included a four cycle formation cycling procedure (see Supplementary Methods) followed by cycling at 25°C for the number of cycles specified in the text at a 1C/2C charge/discharge rate between 2.5 – 4.55 V with a ~ 45 min constant voltage hold at 4.55 V until C/20 current was reached. Note that each of these cycles also included a 10 min rest after both charging and discharging. C-rates were calculated based on a capacity of 215 mAh g^{-1}. After the appropriate number of cycles was performed, the cells were then dismantled in a dry room. The electrodes harvested from these cells were then subject to further electrochemical testing, as detailed below.

All electrochemical tests shown in the text, other than the full cell tests shown in Supplementary Fig. 1, were performed in 2032-type coin cells. A microbalance with μg level

accuracy (XPR2, Mettler Toledo) was used to mass the electrodes. They were assembled in an argon filled glove box using lithium counter electrodes and 1M $LiPF_6$ in EC:DEC (1:1 by weight) electrolyte (LP40, Gotion). They were electrochemically cycled using on a BCS-805 (Bio-logic) potentiostat at the current specified in the text. In Fig. 1a, the cycle numbers given are one higher than the number of cycles conducted in the mini-18650 cell (e.g. the trace labeled cycle 46 underwent formation cycling, 45 normal charge-discharge cycles in the mini-18650, and then 1 more cycle at low rate in a coin cell, which is shown). Note that in Fig. 1a, all samples were cycled between 2.5 and 4.6 V other than the 2^{nd} and 46^{th} cycle, which were charged from 2 V, a negligible change given that less than 0.5 mAh g^{-1} of capacity was observed between 2 and 2.5 V. The sample labeled "Pre-Formation" in Supplementary Fig. 1 was directly fabricated into a 2032-type half cell with no prior formation cycling and included a hold at 4.6 V for 9 mAh g^{-1} of capacity to facilitate the 'activation' process. This sample was an 80% LMR-NMC, 10% carbon, and 10% binder composite by mass. The 2^{nd} cycle data had a negligible hold of 3 mAh g^{-1} at 4.6 V which was excluded from the dQ/dV plot. We note that for the tests shown in Supplementary Figure 54, a different cycling protocol was followed than is listed above. The protocol is explained in detail in that Figure.

X-ray diffraction. X-ray diffraction was performed at beamline 2-1 at the Stanford Synchrotron Radiation Lightsource (SSRL) at 17 keV beam energy. A LaB_6 standard reference material was used to calibrate the energy. The capillaries were 0.5 mm special glass capillaries (Charles Supper) and were loaded inside an argon filled glovebox. The samples were rotated continuously throughout the measurement to avoid preferential orientation effects. The beam was 0.5 mm in width and 1 mm in height. Raw data was recorded using a Pilatus100K detector at a 700 mm distance from the capillary sample.

X-ray absorption. X-ray absorption was conducted in transmission mode on electrodes sealed under a pouch under argon at beamline 2-2 at SSRL. A Si (220) ϕ = 90° monochromator was used and was detuned to 50-60% of maximum intensity to eliminate higher order harmonics. The spectra of Ni, Co, and Mn reference foils were used to calibrate the photon energy by setting the first crossing of zero of the second derivative of the absorbance spectrum to be 8333 eV, 7709 eV, and 6539 eV, respectively. Three ion chambers were used in series to simultaneously measure I0, Isample, and Iref. Spectrum normalization and alignment was performed using the Athena software package[72]. The samples measured for Supplementary Fig. 51 were measured at beamline 11-2 at SSRL with a similar setup. EXAFS analysis and simulation was performed using the Artemis software package (see Supplementary Methods)[72]. All EXAFS data and simulations presented are based upon k^2-weighted EXAFS spectra [$k^2\chi(k)$].

Ultramicrotomy sample preparation. Electrode-sized thin sections were prepared by removing the positive electrode from the coin cell assembly using a coin cell disassembling tool (Hohsen). Once removed, the positive electrode was dipped three times into a vial of DMC to remove any electrolyte or precipitated Li salts and allowed to dry for approximately 10 minutes. The dried electrodes were then cut into smaller pieces, typically into circular sectors. The cut electrodes were placed into a BEEM embedding capsules (size 0) with pointed end down. Subsequently, EpoFix, which is a low viscosity epoxy was poured into the capsule and all remaining gas bubbles were removed from the capsule to ensure a uniform embedding of the sample and adequate penetration of the electrode pores. The epoxy was allowed to set for 24 hours until hardened. Once hardened the embedded samples were trimmed using a Leica Ultramicrotome UC7 equipped with a diamond trimming block (Diatome). The lateral size of the resulting blockface was typically 150-200 μm square or rectangle. Once the block was shaped, sections were

458 created using the Leica Ultramicrotome UC7 and a custom diamond knife (Diatome). The custom
459 diamond knife was created specifically for dry-sectioning of the embedded electrode sample thus
460 removing the need for traditional water-based sample collection. The section thickness was
461 normally set to a nominal thickness of 80 nm, although for preparing the samples shown in
462 Supplementary Figs. 7, 25, and 26, the nominal thickness was set to 60 nm. During sectioning, a
463 constant AC pulse was provided using a CRION antistatic device, in order to ensure sections did
464 not stick to the surface of the knife away from the edge. Sequential sections were collected using
465 a gold coated eyelash controlled using a micromanipulator, which utilized a static DC charge pulse,
466 using the anti-static device, to attract the sections on to the eyelash. Once contacted, the eyelash
467 was used to create a large ribbon consisting sequential sections by keeping the ribbon taut while
468 new sections were cut. Once a sufficiently long ribbon was created, a second micromanipulator
469 holding a TEM sample grid was brought into contact with the sample ribbon and then an DC pulse
470 was used to detach the sample from the eyelash and attach it to the grid. From there, mesh grid
471 samples were stored in a grid box inside of a glovebox until the X-ray microscopy measurements
472 were performed. The reasonable agreement of the spatially-averaged Mn oxidation state in the
473 sectioned samples ($Mn^{3.80+}$ in Fig. 4a) with Mn oxidation states found from both K- and L_3-edge
474 spectroscopy of non-sectioned samples (Fig. 1a and Supplementary Fig. 16) indicates that
475 sectioning does not significantly alter the chemical state of the discharged electrodes. Likewise,
476 the significant presence of oxidized oxygen (Fig. 5c) in the sectioned charged samples[2,68,73]
477 suggests that sectioning is unlikely to significantly alter the chemical state of the charged samples.
478 Based on the qualitative similarities in, for example, Supplementary Figs. 26 and 27, it is likely
479 that many primary particles remain intact after the ultramicrotomy process. Still, the cutting of
480 some primary particles may occur and cannot be excluded. This sample preparation method was

used for all images of the material shown in the main text with the sole exception of the pristine particles in Fig. 2a.

Dispersed sample preparation. Samples prepared via sonication and dispersion were removed from coin cells as above and then prepared as reported previously[2]. These samples account for the spectra in Fig. 1d (which are taken from the images shown in Supplementary Figure 16) as well as the image of the pristine sample in Fig. 2a and all samples in Supplementary Figures 16,17,39,41,43,44,50 (pristine and Mn_2O_3), and 52.

Scanning transmission x-ray microscopy. Sectioned and dispersed samples were loaded onto 3 mm Si_3N_4 TEM grids (Norcada), with some measurements being taken on 3 mm copper TEM grids with a formvar film coated with a layer of carbon (Ted Pella, mesh 100). The samples were transported sealed under argon to the Advanced Light Source (ALS) at Lawrence Berkeley National Laboratory. STXM measurements were performed at beamlines 11.0.2.2 and 7.0.1.2 using a zone plate with outer zone width of 45 nm. Images at different X-ray energies were aligned using the aXis2000 software package when possible and a custom Python script when necessary. The energy of the beam was calibrated at each edge using a reference sample, generally the pristine LMR material. Analysis was performed using custom MATLAB software.

X-ray Ptychography. Ptychography measurements were performed at beamline 7.0.1.2 at the ALS and were taken almost exclusively in double exposure mode to allow for maximum spatial resolution while avoiding detector saturation. The scan step size was set to ~ 40 nm, with a reconstructed image pixel size of ~ 5 nm. Supplementary Fig. 52 and 53 show that the samples' chemical states are not significantly altered by the high X-ray dose of ptychography measurements.

Scanning electron microscopy (SEM). Samples for scanning electron microscopy were prepared by light sonication (~ 2 min) in isopropanol followed by being dropcast on small sections of aluminum foil. Scanning electron micrographs were recorded on a Sirion SEM (FEI) at Stanford Nano Shared Facilities (SNSF).

Inductively coupled plasma mass spectrometry (ICP-MS). ICP-MS was performed on a Thermo Scientific XSERIES 2 ICP-MS at Stanford's Environmental Measurements Facility. Samples were prepared by washing with anhydrous dimethyl carbonate after cell disassembly, and then by dissolving the sample in 2% HNO_3 in the presence of ~ 1% H_2O_2. Although the carbon did not dissolve, the elemental composition found from an electrode was nearly identical to that found of the pristine material, confirming the robustness of the preparation method. The quantity of each element present was found using a calibration curve generated by preparing seven standard solutions of known concentrations. Stock solutions of Li, Ni, Mn, and Co dissolved in 2% HNO_3 (Inorganic Ventures) were used to prepare the standard solutions.

Pycnometry. Density measurements were conducted using a 1 cm^3 AccuPyc II 1340 automatic gas pycnometer (Micromeritics) using a 0.1 cm^3 insert and 99.9999% pure He gas (Praxair). The volume of the insert and the expansion chamber were calibrated using a 0.718541 cm^3 standard ball bearing (Micromeritics). Ten or more repeat measurements with cap removal/replacement were made of each sample, with the average and standard error reported in Fig. 3b.

Neutron diffraction. ~ 500 mg of pristine material was loaded in a 3 mm vanadium can, sealed under argon, and transported the POWGEN beamline at Oak Ridge National Laboratory.

The diffraction pattern was then collected at room temperature in high resolution mode using a beam of neutrons with a center wavelength of 1.5 Å.

Annealing of Cycled Electrodes. The annealing of cycled electrodes was conducted by heating the cycled electrode, which was first discharged to and held at 2.5 V vs. Li/Li^+ for ~ 6 hrs, at 150 °C for 18 hr in a 100% O_2 gas environment. The electrode did not delaminate during this process, and therefore the electrochemical test shown in Supplementary Fig. 31 was conducted simply by reassembling a coin cell with the electrode following heat treatment.

Transmission Electron Microscopy. Scanning TEM Annular Dark Field (STEM-ADF) images were taken using a FEI Titan Environment TEM operating at 300 kV with an image corrector. The probe size was 0.5 nm and the convergence and collection semi-angles were 9.3 mrad and 19 – 25 mrad, respectively. Selected area diffraction patterns (SADP) were collected using the same TEM. High resolution transmission electron microscopy (HRTEM) images (Supplementary Figures 8 and 9) were taken on a different TEM (FEI Tecnai G2 F20 X-TWIN), which was operated at an accelerating voltage of 200 kV.

Focused Ion Beam (FIB) Sectioning. For the FIB-SEM-prepared TEM lamella, the work was done on the FEI Helios 600i DualBeam Focused Ion Beam/Scanning Electron Microscope at the Stanford Nano Shared Facilities. Electron-beam and then ion-beam platinum deposition was performed sequentially to planarize the region to be extracted, at approximately 300nm and 500nm thicknesses, each. Trench cuts were milled in front of and behind the protected region to expose the cross-section to be extracted. The lamella was polished down to about 1 micron thickness for extraction while at 30 kV and with the sample orthogonal to the ion beam. Re-orienting the sample normal to the electron beam, an “U”-cut was made cleanly

through to define the edges of the lamella, leaving two tabs at either top edge. An Omniprobe AutoProbe 200 standard tungsten tip was inserted and welded to one top corner using ion-beam deposited platinum. The lamella was then severed from the substrate and subsequently attached cantilever-style to the edge of a copper Omniprobe lift-out grid post, also using ion-beam deposited platinum, and the needle was severed to release. The lamella was then further polished with the ion beam, both front and back, to sub-200 nm thickness while at 30 kV and an additional ±1.5º tilt off-normal to strive for parallel sidewalls. Final polishing was done at 5 kV and ±3º off-normal tilt to minimize amorphization damage and achieve electron-transparency. This sample preparation method was used to create the images shown in Supplementary Figures 8 and 9.

References

1. Croy, J. R., Balasubramanian, M., Gallagher, K. G. & Burrell, A. K. Review of the U.S. Department of Energy's "Deep Dive" Effort to Understand Voltage Fade in Li- and Mn-Rich Cathodes. *Acc. Chem. Res.* **48**, 2813–2821 (2015).
2. Gent, W. E. *et al.* Coupling between oxygen redox and cation migration explains unusual electrochemistry in lithium-rich layered oxides. *Nat. Commun.* **8**, 2091 (2017).
3. Sathiya, M. *et al.* Origin of voltage decay in high-capacity layered oxide electrodes. *Nat. Mater.* **14**, 230–238 (2015).
4. Abdellahi, A., Urban, A., Dacek, S. & Ceder, G. The Effect of Cation Disorder on the Average Li Intercalation Voltage of Transition-Metal Oxides. *Chem. Mater.* **28**, 3659–3665 (2016).
5. Kleiner, K. *et al.* Origin of high capacity and poor cycling stability of Li-rich layered oxides - A long-duration in situ synchrotron powder diffraction study. *Chem. Mater.* **30**, 3656–3667 (2018).
6. Mohanty, D. *et al.* Unraveling the voltage-fade mechanism in high-energy-density lithium-ion batteries: Origin of the tetrahedral cations for spinel conversion. *Chem. Mater.* **26**, 6272–6280 (2014).
7. Liu, H. *et al.* Unraveling the Rapid Performance Decay of Layered High-Energy Cathodes: From Nanoscale Degradation to Drastic Bulk Evolution. *ACS Nano* **12**, 2708–2718 (2018).
8. Castel, E., Berg, E. J., El Kazzi, M., Novák, P. & Villevieille, C. Differential electrochemical mass spectrometry study of the interface of x Li2MnO3·(1- x)LiMO2 (M = Ni, Co, and Mn) material as a positive electrode in li-ion batteries. *Chem. Mater.* **26**, 5051–5057 (2014).
9. Strehle, B. *et al.* The Role of Oxygen Release from Li- and Mn-Rich Layered Oxides during the First Cycles Investigated by On-Line Electrochemical Mass Spectrometry. *J. Electrochem. Soc.* **164**, A400–A406 (2017).
10. Hong, J. *et al.* Critical role of oxygen evolved from layered Li-Excess metal oxides in lithium rechargeable batteries. *Chem. Mater.* **24**, 2692–2697 (2012).
11. Yan, P. *et al.* Injection of oxygen vacancies in the bulk lattice of layered cathodes. *Nat. Nanotechnol.* **14**, 602–608 (2019).
12. Hu, E. *et al.* Evolution of redox couples in Li- and Mn-rich cathode materials and mitigation of voltage fade by reducing oxygen release. *Nat. Energy* **3**, 690–698 (2018).
13. Wang, C. & Zhang, J. Structural and Chemical Evolution of Li- and Mn-Rich Layered Cathode Material. *Chem. Mater.* **27**, 1381–1390 (2015).
14. Zhu, Z. *et al.* Gradient Li-rich oxide cathode particles immunized against oxygen release by a molten salt treatment. *Nat. Energy* **4**, 1049–1058 (2019).
15. Gu, M. *et al.* Formation of the spinel phase in the layered composite cathode used in Li-Ion batteries. *ACS Nano* **7**, 760–767 (2013).
16. Teufl, T., Strehle, B., Müller, P., Gasteiger, H. A. & Mendez, M. A. Oxygen Release and Surface Degradation of Li- and Mn-Rich Layered Oxides in Variation of the Li2MnO3 Content. *J. Electrochem. Soc.* **165**, A2718–A2731 (2018).
17. Qian, D., Xu, B., Chi, M. & Meng, Y. S. Uncovering the roles of oxygen vacancies in cation migration in lithium excess layered oxides. *Phys. Chem. Chem. Phys.* **16**, 14665–14668 (2014).

18. Mohanty, D. *et al.* Correlating cation ordering and voltage fade in a lithium-manganese-rich lithium-ion battery cathode oxide: A joint magnetic susceptibility and TEM study. *Phys. Chem. Chem. Phys.* **15**, 19496–19509 (2013).
19. Boulineau, A., Simonin, L., Colin, J. F., Bourbon, C. & Patoux, S. First evidence of manganese-nickel segregation and densification upon cycling in Li-rich layered oxides for lithium batteries. *Nano Lett.* **13**, 3857–3863 (2013).
20. Koga, H. *et al.* Reversible Oxygen Participation to the Redox Processes Revealed for Li1.20Mn0.54Co0.13Ni0.13O2. *J. Electrochem. Soc.* **160**, A786–A792 (2013).
21. Koga, H. *et al.* Different oxygen redox participation for bulk and surface: A possible global explanation for the cycling mechanism of Li1.20Mn0.54Co0.13Ni0.13O2. *J. Power Sources* **236**, 250–258 (2013).
22. Gallagher, K. G. *et al.* Correlating hysteresis and voltage fade in lithium- and manganese-rich layered transition-metal oxide electrodes. *Electrochem. commun.* **33**, 96–98 (2013).
23. Dau, H., Liebisch, P. & Haumann, M. X-ray absorption spectroscopy to analyze nuclear geometry and electronic structure of biological metal centers-potential and questions examined with special focus on the tetra-nuclear manganese complex of oxygenic photosynthesis. *Anal. Bioanal. Chem.* **376**, 562–583 (2003).
24. Yabuuchi, N., Yoshii, K., Myung, S.-T., Nakai, I. & Komaba, S. Detailed Studies of a High-Capacity Electrode Material for Rechargeable Batteries, Li2MnO3−LiCo1/3Ni1/3Mn1/3O2. *J. Am. Chem. Soc.* **133**, 4404–4419 (2011).
25. Luo, K. *et al.* Charge-compensation in 3d-transition-metal-oxide intercalation cathodes through the generation of localized electron holes on oxygen. *Nat. Chem.* **8**, 684–691 (2016).
26. Lee, J. *et al.* Mitigating oxygen loss to improve the cycling performance of high capacity cation-disordered cathode materials. *Nat. Commun.* **8**, 981 (2017).
27. Bluhm, H. *et al.* Soft X-ray microscopy and spectroscopy at the molecular environmental science beamline at the Advanced Light Source. *J. Electron Spectros. Relat. Phenomena* **150**, 86–104 (2006).
28. Celestre, R. *et al.* Nanosurveyor 2: A Compact Instrument for Nano-Tomography at the Advanced Light Source. *J. Phys. Conf. Ser.* **849**, 6–10 (2017).
29. Yu, Y. S. *et al.* Dependence on Crystal Size of the Nanoscale Chemical Phase Distribution and Fracture in LixFePO4. *Nano Lett.* **15**, 4282–4288 (2015).
30. Shapiro, D. A. *et al.* Chemical composition mapping with nanometre resolution by soft X-ray microscopy. *Nat. Photonics* **8**, 765–769 (2014).
31. Hong, J. *et al.* Metal–oxygen decoordination stabilizes anion redox in Li-rich oxides. *Nat. Mater.* **18**, 256–265 (2019).
32. Yang, F. *et al.* Nanoscale morphological and chemical changes of high voltage lithium-manganese rich NMC composite cathodes with cycling. *Nano Lett.* **14**, 4334–4341 (2014).
33. Genevois, C. *et al.* Insight into the atomic structure of cycled lithium-rich layered oxide Li1.20Mn0.54Co0.13Ni0.13O2using HAADF STEM and electron nanodiffraction. *J. Phys. Chem. C* **119**, 75–83 (2015).
34. Li, J., Shunmugasundaram, R., Doig, R. & Dahn, J. R. In Situ X-ray Diffraction Study of Layered Li-Ni-Mn-Co Oxides: Effect of Particle Size and Structural Stability of Core-Shell Materials. *Chem. Mater.* **28**, 162–171 (2016).
35. Huang, Y. *et al.* Thermal Stability and Reactivity of Cathode Materials for Li-Ion Batteries. *ACS Appl. Mater. Interfaces* **8**, 7013–7021 (2016).

36. Bak, S. M. *et al.* Structural changes and thermal stability of charged LiNixMnyCozO2 cathode materials studied by combined in situ time-resolved XRD and mass spectroscopy. *ACS Appl. Mater. Interfaces* **6**, 22594–22601 (2014).
37. Xu, B., Fell, C. R., Chi, M. & Meng, Y. S. Identifying surface structural changes in layered Li-excess nickel manganese oxides in high voltage lithium ion batteries: A joint experimental and theoretical study. *Energy Environ. Sci.* **4**, 2223–2233 (2011).
38. Lin, F. *et al.* Surface reconstruction and chemical evolution of stoichiometric layered cathode materials for lithium-ion batteries. *Nat. Commun.* **5**, 3529 (2014).
39. Nemudry, A., Goldberg, E. L., Aguirre, M. & Alario-Franco, M. Á. Electrochemical topotactic oxidation of nonstoichiometric perovskites at ambient temperature. *Solid State Sci.* **4**, 677–690 (2002).
40. Mefford, J. T. *et al.* Water electrolysis on La1-xSrxCoO3-δ perovskite electrocatalysts. *Nat. Commun.* **7**, 11053 (2016).
41. Mefford, J. T., Hardin, W. G., Dai, S., Johnston, K. P. & Stevenson, K. J. Anion charge storage through oxygen intercalation in LaMnO3 perovskite pseudocapacitor electrodes. *Nat. Mater.* **13**, 726–732 (2014).
42. Kudo, T., Obayashi, H. & Gejo, T. Electrochemical Behavior of the Perovskite-Type Nd1-xSrxCoO3in an Aqueous Alkaline Solution. *J. Electrochem. Soc.* **122**, 159–163 (1975).
43. House, R. A. *et al.* First-cycle voltage hysteresis in Li-rich 3d cathodes associated with molecular O2 trapped in the bulk. *Nat. Energy* **5**, 777–785 (2020).
44. Lee, E. & Persson, K. A. Structural and Chemical Evolution of the Layered Li-Excess LixMnO3 as a Function of Li Content from First-Principles Calculations. *Adv. Energy Mater.* **4**, 1400498 (2014).
45. Gerbig, O., Merkle, R. & Maier, J. Electrical transport and oxygen exchange in the superoxides of potassium, rubidium, and cesium. *Adv. Funct. Mater.* **25**, 2552–2563 (2015).
46. Royer, S., Duprez, D. & Kaliaguine, S. Oxygen mobility in LaCoO3 perovskites. *Catal. Today* **112**, 99–102 (2006).
47. Singer, A. *et al.* Nucleation of dislocations and their dynamics in layered oxide cathode materials during battery charging. *Nat. Energy* **3**, 641–647 (2018).
48. Tran, N. *et al.* Mechanisms Associated with the "Plateau" Observed at High Voltage for the Overlithiated Li 1.12 (Ni 0.425 Mn 0.425 Co 0.15) 0.88 O 2 System. *Chem. Mater.* **20**, 4815–4825 (2008).
49. Armstrong, A. R. *et al.* Demonstrating Oxygen Loss and Associated Structural Reorganization in the Lithium Battery Cathode Li[Ni 0.2 Li 0.2 Mn 0.6]O 2. *J. Am. Chem. Soc.* **128**, 8694–8698 (2006).
50. Wu, Y. & Manthiram, A. Effect of surface modifications on the layered solid solution cathodes (1 - z) Li[Li1/3Mn2/3]O2 - (z) Li[Mn0.5 - yNi0.5 - yCo2y]O2. *Solid State Ionics* **180**, 50–56 (2009).
51. Yin, W. *et al.* Structural evolution at the oxidative and reductive limits in the first electrochemical cycle of Li1.2Ni0.13Mn0.54Co0.13O2. *Nat. Commun.* **11**, 1252 (2020).
52. Zhang, Z. *et al.* Cathode-Electrolyte Interphase in Lithium Batteries Revealed by Cryogenic Electron Microscopy. *Matter* **4**, 302–312 (2021).
53. Shunmugasundaram, R., Senthil Arumugam, R. & Dahn, J. R. High capacity li-rich positive electrode materials with reduced first-cycle irreversible capacity loss. *Chem. Mater.* **27**, 757–767 (2015).

54. Qiu, B. *et al.* Metastability and Reversibility of Anionic Redox-Based Cathode for High-Energy Rechargeable Batteries. *Cell Reports Phys. Sci.* **1**, 100028 (2020).
55. Mortemard de Boisse, B. *et al.* Highly Reversible Oxygen-Redox Chemistry at 4.1 V in Na 4/7−x[□1/7Mn6/7]O2 (□: Mn Vacancy). *Adv. Energy Mater.* **8**, 1800409 (2018).
56. McCalla, E., Rowe, A. W., Camardese, J. & Dahn, J. R. The role of metal site vacancies in promoting Li-Mn-Ni-O layered solid solutions. *Chem. Mater.* **25**, 2716–2721 (2013).
57. Qiao, R. *et al.* Direct Experimental Probe of the Ni(II)/Ni(III)/Ni(IV) Redox Evolution in LiNi0.5Mn1.5O4 Electrodes. *J. Phys. Chem. C* **119**, 27228–27233 (2015).
58. Fell, C. R. *et al.* Correlation between oxygen vacancy, microstrain, and cation distribution in lithium-excess layered oxides during the first electrochemical cycle. *Chem. Mater.* **25**, 1621–1629 (2013).
59. Zheng, J. *et al.* Functioning mechanism of AlF3 coating on the Li- and Mn-rich cathode materials. *Chem. Mater.* **26**, 6320–6327 (2014).
60. Mohanty, D. *et al.* Modification of Ni-Rich FCG NMC and NCA Cathodes by Atomic Layer Deposition: Preventing Surface Phase Transitions for High-Voltage Lithium-Ion Batteries. *Sci. Rep.* **6**, 26532 (2016).
61. Eum, D. *et al.* Voltage decay and redox asymmetry mitigation by reversible cation migration in lithium-rich layered oxide electrodes. *Nat. Mater.* **19**, 419–428 (2020).
62. Maitra, U. *et al.* Oxygen redox chemistry without excess alkali-metal ions in Na2/3[Mg0.28Mn0.72]O2. *Nat. Chem.* **10**, 288–295 (2018).
63. House, R. A. *et al.* Superstructure control of first-cycle voltage hysteresis in oxygen-redox cathodes. *Nature* **577**, 502–508 (2019).
64. Gent, W. E. *et al.* Persistent State-of-Charge Heterogeneity in Relaxed, Partially Charged Li1−xNi1/3Co1/3Mn1/3O2Secondary Particles. *Adv. Mater.* **28**, 6631–6638 (2016).
65. Liu, J. *et al.* Electrochemical performance studies of Li-rich cathode materials with different primary particle sizes. *J. Power Sources* **251**, 208–214 (2014).
66. Ruess, R. *et al.* Influence of NCM particle cracking on Kinetics of Lithium-ion batteries with liquid or solid electrolyte. *J. Electrochem. Soc.* **167**, 100532 (2020).
67. Li, J. *et al.* Comparison of single crystal and polycrystalline LiNi0.5Mn0.3Co0.2O2 positive electrode materials for high voltage Li-ion cells. *J. Electrochem. Soc.* **164**, A1534–A1544 (2017).
68. Assat, G., Iadecola, A., Foix, D., Dedryvère, R. & Tarascon, J.-M. Direct quantification of anionic redox over long cycling of li-rich nmc via hard x-ray photoemission spectroscopy. *ACS Energy Lett.* **3**, 2721–2728 (2018).
69. Qiu, B. *et al.* Gas-solid interfacial modification of oxygen activity in layered oxide cathodes for lithium-ion batteries. *Nat. Commun.* **7**, 12108 (2016).
70. Kim, S., Cho, W., Zhang, X., Oshima, Y. & Choi, J. W. A stable lithium-rich surface structure for lithium-rich layered cathode materials. *Nat. Commun.* **7**, 13598 (2016).
71. Lu, Z. & Dahn, J. R. In Situ X-Ray Diffraction Study of P2-Na2/3[Ni 1/3Mn2/3]O2. *J. Electrochem. Soc.* **148**, A1225 (2001).
72. Ravel, B. & Newville, M. ATHENA, ARTEMIS, HEPHAESTUS: Data analysis for X-ray absorption spectroscopy using IFEFFIT. *J. Synchrotron Radiat.* **12**, 537–541 (2005).
73. Dai, K. *et al.* High Reversibility of Lattice Oxygen Redox Quantified by Direct Bulk Probes of Both Anionic and Cationic Redox Reactions. *Joule* **3**, 518–541 (2018).

Acknowledgements

The battery component of this work was supported by the Assistant Secretary for Energy Efficiency and Renewable Energy, Office of Vehicle Technologies, Battery Materials Research Program, US Department of Energy (DOE), and by Samsung Advanced Institute of Technology Global Research Outreach program. STXM and X-ray ptychography development was supported by DOE, Office of Basic Energy Sciences, Division of Materials Sciences and Engineering (contract DE-AC02-76SF00515). This research used resources of the Advanced Light Source, a DOE Office of Science User Facility under contract no. DE-AC02-05CH11231. This work was partially supported by STROBE: a National Science Foundation Science and Technology Center under award DMR1548924. Use of the Stanford Synchrotron Radiation Lightsource, SLAC National Accelerator Laboratory, is supported by the U.S. Department of Energy, Office of Science, Office of Basic Energy Sciences under Contract No. DE-AC02-76SF00515. A portion of this research used resources at the Spallation Neutron Source, a DOE Office of Science User Facility operated by the Oak Ridge National Laboratory. Part of this work was performed at the Stanford Nano Shared Facilities (SNSF), supported by the National Science Foundation under award ECCS-1542152. P.M.C. acknowledges support through the Stanford Graduate Fellowship as a Winston and Fu-Mei Chen fellow and through the National Science Foundation Graduate Research Fellowship under Grant No. DGE-1656518. W.E.G. was supported additionally by the Advanced Light Source Doctoral Fellowship. Y.L. and R.S. acknowledge the financial support from the Toyota Research Institute – Accelerated Materials Design and Discovery (TRI-AMDD) program (Stanford University). We thank Laura Echavez, Laura Schelhas, Tyler Mefford, Matthew Lattimer, and Bjoern Enders for helpful discussions and/or experimental support. We

771 acknowledge Richard Chin for performing FIB electrode cross-sectioning for TEM experiments.
772 We also acknowledge Roy Kim for experimental TEM support and helpful discussions.

773 **Author Contributions**

774 P.M.C., S.S.K., W.E.G., D.A.S., M.F.T., and W.C.C. conceived the study. S.S.K. and E.K.
775 performed the ultramicrotomy sectioning. P.M.C., S.S.K., W.E.G., Y.-S.Y. and D.A.S. collected
776 ex situ STXM and ptychography images and analyzed the data. P.M.C., K.L., and K.H.S.
777 collected SXRD data. P.M.C. collected ND data. P.M.C., K.L., K.H.S., and M.F.T. analyzed the
778 diffraction data. S.-J.A. synthesized the material and cycled the mini-18650 cells. P.M.C.
779 performed the ICP-MS, SEM, and pycnometry experiments. P.M.C. collected transition metal
780 K-edge spectra and K.L., W.E.G., and M.F.T. contributed to the interpretation. P.M.C and
781 W.C.C. developed the diffusion and two-phase core-shell models used. Y. L. and X.X. collected
782 TEM images. Y.L., X.X., P.M.C., A.F.M., R.S., and W.C.C. analyzed the TEM data. P.M.C,
783 W.C.C., and M.F.T. wrote the manuscript and all authors revised the manuscript.

784 **Competing Interests**

785 The authors declare no competing interests.

786 **Data Availability**

787 Data supporting all main text figures can be found at https://doi.org/10.5281/zenodo.4697951.
788 Data supporting all supplementary information figures can be found at
789 https://doi.org/10.5281/zenodo.4697955.

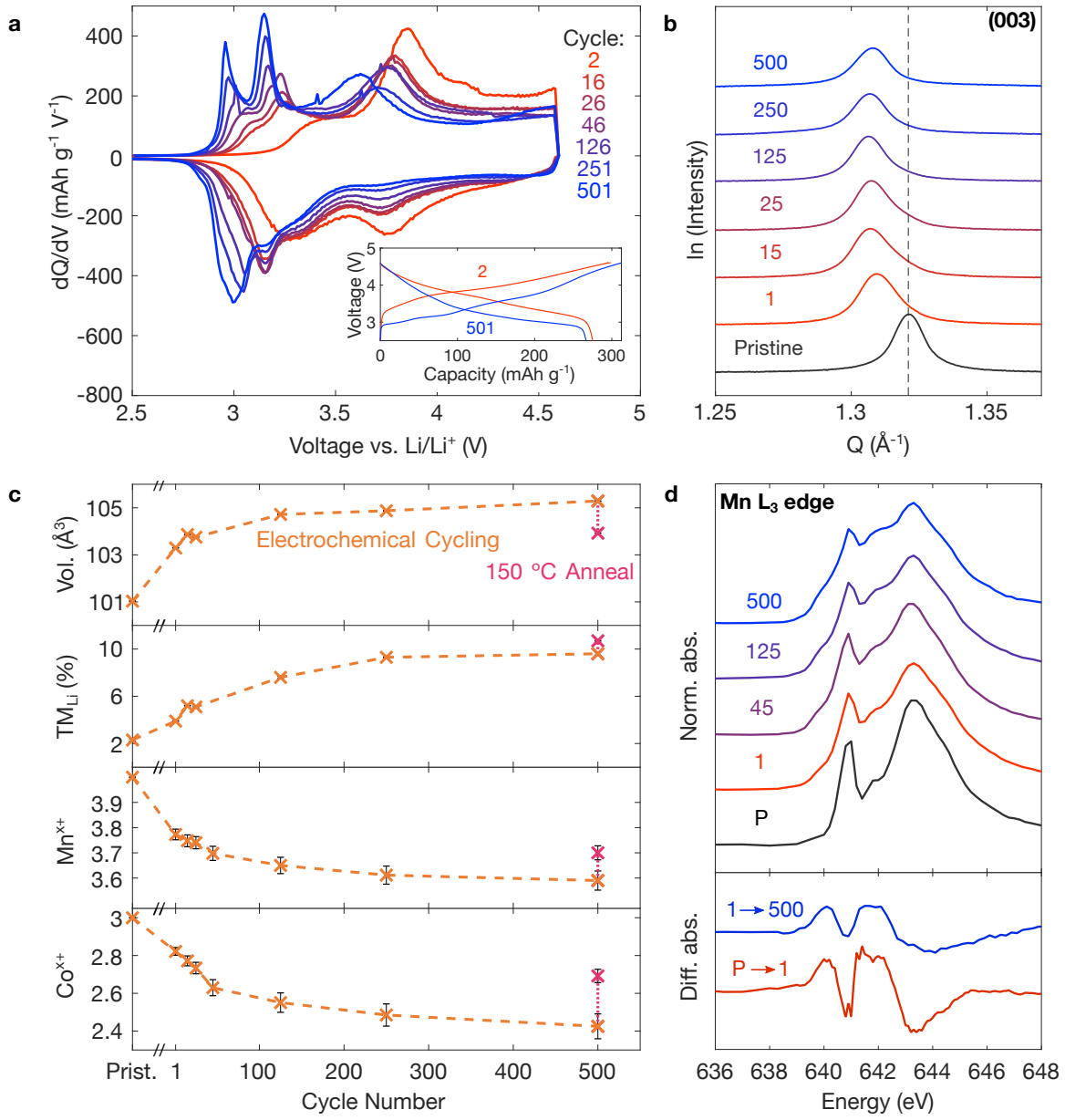

Figure 1. Electrochemical voltage depression linked to cation disordering and TM reduction. a Electrochemical differential capacity plots taken at ~ 4 mA g^{-1}. The inset shows that the discharge capacity remains at ~ 96% of its initial value even after 500 cycles. **b** (003) peak plotted on a logarithmic scale after varying numbers of cycles with an absence of secondary peaks, indicating that the bulk material remains a single phase upon cycling. **c** The voltage depression upon cycling is correlated with an increase in the unit cell volume (Vol.), an increase in the TM occupancy in the Li layer (TM_{Li}), and the reduction of the average TM oxidation state (Co^{x+} and Mn^{x+}). Error bars are from Rietveld refinement (Supplementary Fig. 3) and the uncertainty in the edge position vs. oxidation state slope (Supplementary Fig. 11). The TM reduction and lattice volume expansion which occur over cycling can be partially reversed by annealing the cycled electrode at 150 °C. **d** Transmission-based Mn L_3-edge spectra obtained through STXM showing significant changes over 500 cycles. The differential spectra reveal that a similar change takes place between the 1st and 500th cycle as that which occurs between the pristine material and 1st cycle. Raw data for this figure is available (see Data Availability).

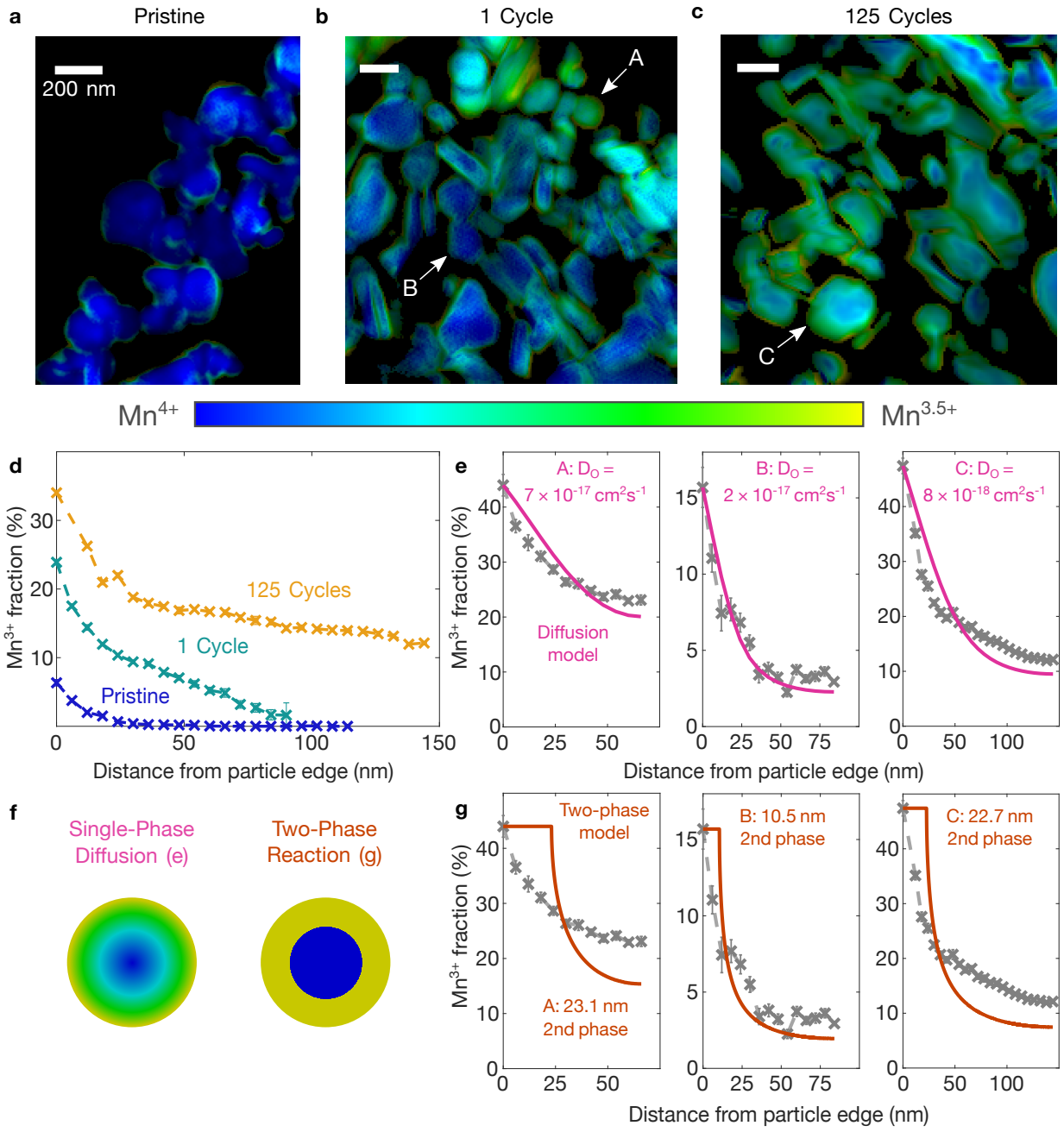

Figure 2. Spatial dependence of the Mn oxidation state within primary particles. X-ray ptychography images of the **a** pristine material and material after **b** 1 cycle and **c** 125 cycles are shown. The scale bar in each image is 200 nm. **d** The Mn^{3+} content as a function of distance from the particle edge. **e** The Mn^{3+} spatial distribution in selected particles (with minimal particle overlap) fit with a diffusion profile and individual chemical diffusion coefficient. The results suggest an overall oxygen chemical diffusion coefficient of ~ 10^{-17} cm^2s^{-1}. **f** Schematic illustration of two possible mechanisms which can give rise to a Mn^{3+} concentration which is lower in the bulk than on the surface. **g** The Mn^{3+} spatial distribution in individual particles fit with a two-phase core-shell model. The fits using this model are qualitatively and quantitatively poor. Error bars are based on the weighted standard error of the Mn^{3+} concentration of the pixels contributing to each data point. Raw data for this figure is available (see Data Availability).

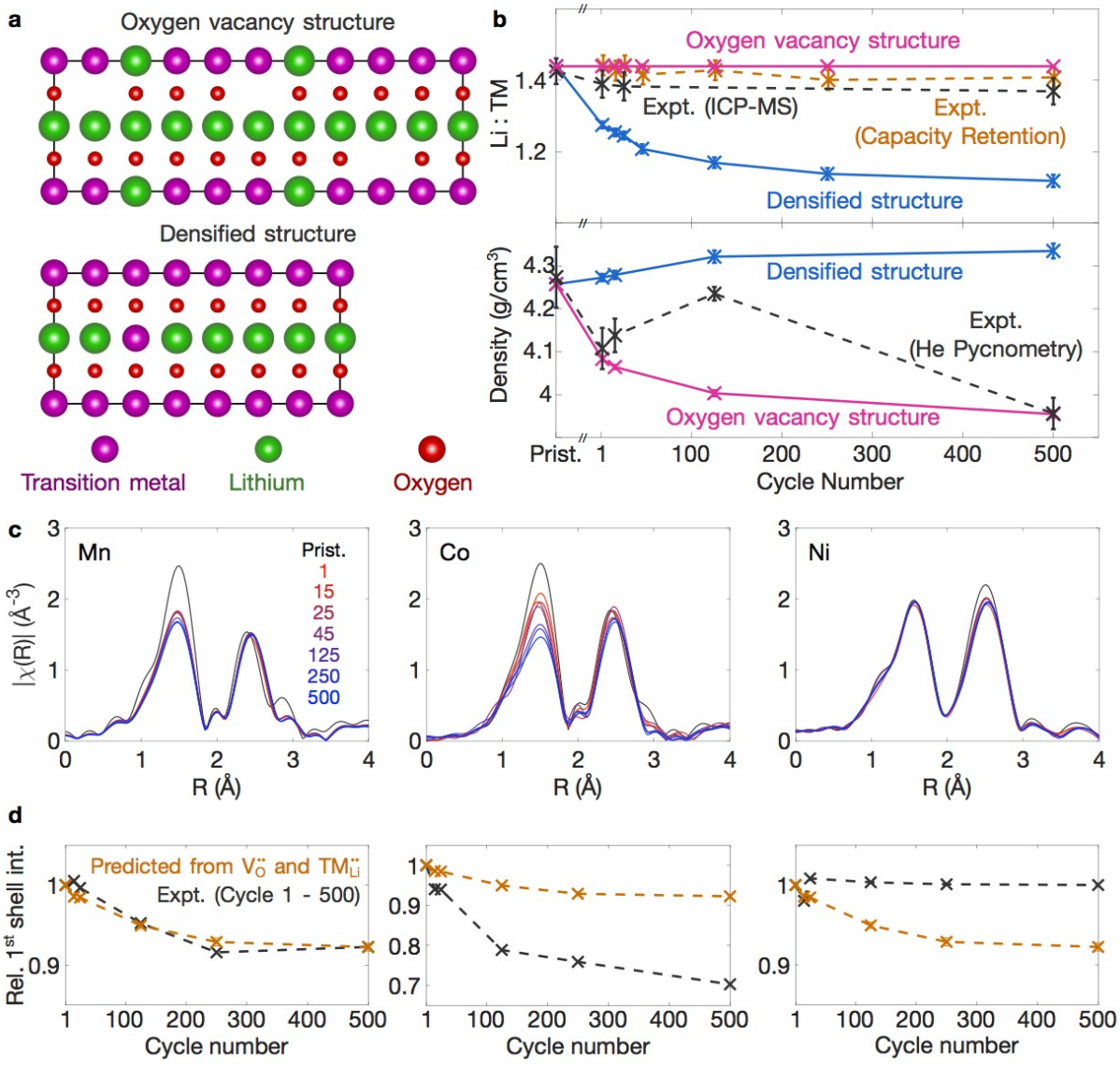

Figure 3. Structural Consequences of Oxygen Release. a Graphical depiction of the two possible structures after 500 cycles discussed in the text. The initial structure in this illustration (not shown) is identical to the vacancy structure but with a full oxygen sublattice. Both structures depicted here would have an identical average TM oxidation state of 2.75+. **b** ICP-MS, capacity retention, and helium pycnometry density measurements with the pink and blue lines representing the expected measurement values if all of the oxygen release were accompanied by the formation of oxygen vacancies or densification, respectively. All three measurements indicate that the majority of the oxygen release causes the formation of oxygen vacancies. ICP-MS and pycnometry error bars are based on the standard error of repeat measurements. Capacity retention error bars are based on an estimated 5 mAh g^{-1} uncertainty in discharge capacity. Error bars for the structure models are propagated from the uncertainty in the edge position vs. oxidation state slope (Supplementary Fig. 11) **c** EXAFS data at the TM K edge as a function of cycle number showing a decrease in the first shell scattering intensity with cycling for Mn and Co, but not Ni. **d** A quantitative comparison of the relative changes in first shell scattering intensity (approximated by the maximum value of $|\chi(R)|$) at the Mn, Co, and Ni K edge with that which would be predicted from the presence of both $V_O^{\cdot\cdot}$ and $TM_{Li}^{\cdot\cdot}$ defects alone. Error bars in the predicted values are

propagated from uncertainty in the $V_O^{\cdot\cdot}$ and $TM_{Li}^{\cdot\cdot}$ concentrations. Raw data for this figure is available (see Data Availability).

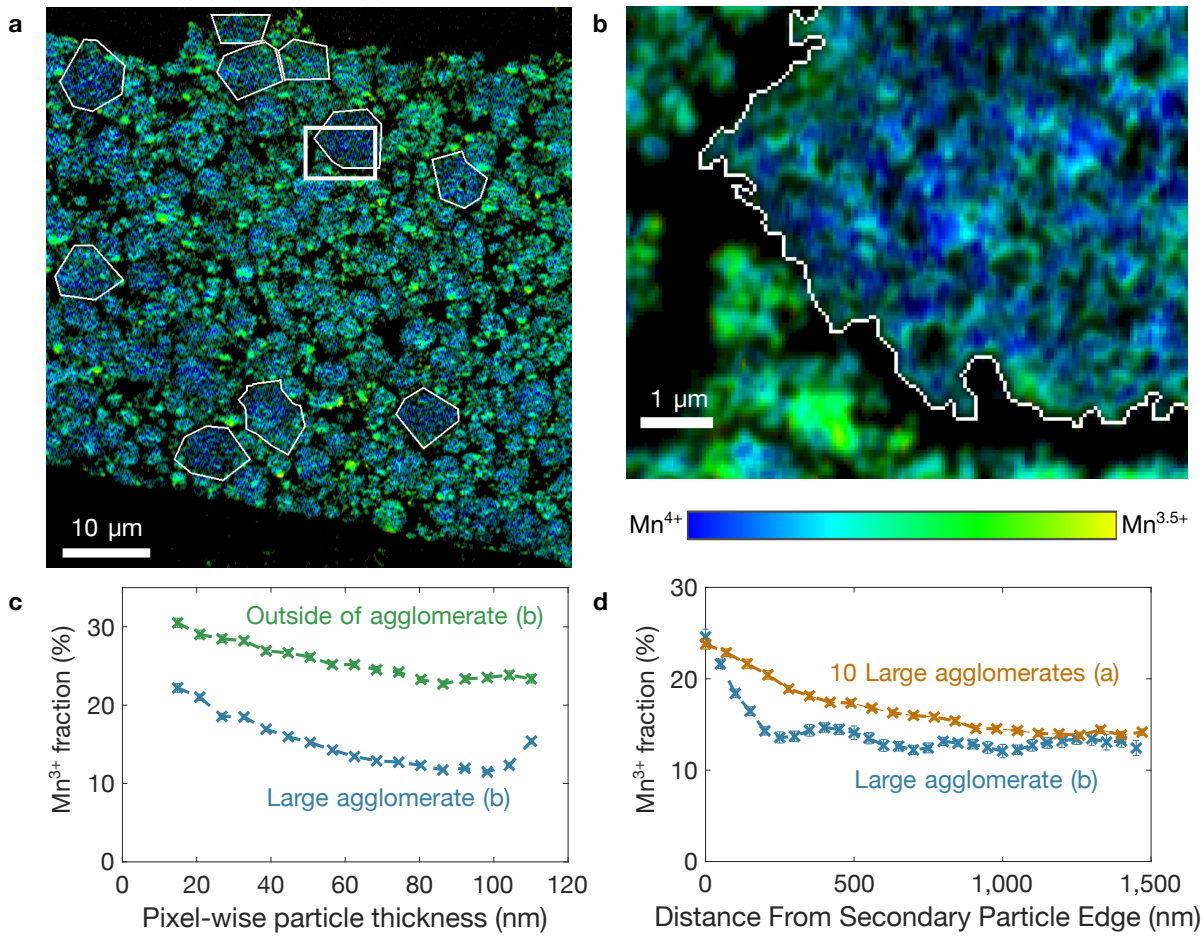

Figure 4. Oxidation state heterogeneity on the secondary particle scale. All samples in this figure are taken after 1 cycle followed by discharging to 2.5 V vs. Li/Li^+ and holding for ~ 6 h. **a** Image with the field of view covering the entire electrode thickness (~ 40 µm). Ten large agglomerates are outlined in white. **b** A single large agglomerate (top right of image, outlined in white) that is significantly more oxidized than the surrounding areas. This image, taken at finer resolution than Fig. 4a, corresponds to the region in the thick white rectangle in Fig. 4a. **c** The trend of a relatively more oxidized large agglomerate is maintained even at a fixed particle thickness, implying that a primary particle of identical size and shape will be more oxidized within the large agglomerate than outside of it. **d** The primary particles at the exterior of large agglomerates are more reduced than the primary particles in interior. Error bars are based on the weighted standard error of the Mn^{3+} concentration of the pixels contributing to each data point. Raw data for this figure is available (see Data Availability).

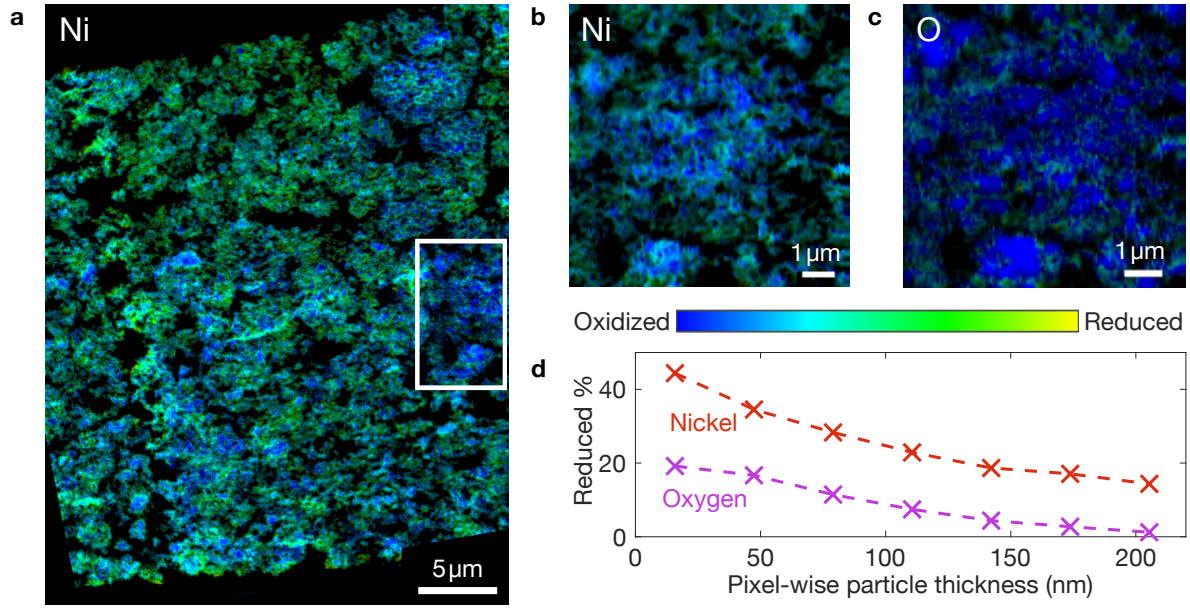

Figure 5. Oxidation State Heterogeneity in the Charged State. All samples in this figure are taken after 125 cycles following by charging to 4.6 V vs. Li/Li^+ and holding for ~ 6 h. **a** Distribution of the Ni oxidation state with the field of view covering the entire electrode thickness. The area in the white boxed region was imaged a second time with finer energy resolution, which is shown in Fig. 5b,c. **b** Distribution of the Ni oxidation state in a large secondary particle. **c** Distribution of the O oxidation state in a large secondary particle. **d** Fraction of the reduced component (see Supplementary Fig. 42) present as a function of particle thickness for Fig. 5b,c. The results indicate that the surface of the material is not able to achieve as high of an oxidation state as the bulk. Error bars are based on the weighted standard error of the Mn^{3+} concentration of the pixels contributing to each data point. Raw data for this figure is available (see Data Availability).